



NRC Publications Archive Archives des publications du CNRC

Taking a little off the top : nanorod array morphology and growth studied by focused ion beam tomography

Krause, Kathleen M.; Vick, Douglas W.; Malac, Marek; Brett, Michael J.

This publication could be one of several versions: author's original, accepted manuscript or the publisher's version. / La version de cette publication peut être l'une des suivantes : la version prépublication de l'auteur, la version acceptée du manuscrit ou la version de l'éditeur.

For the publisher's version, please access the DOI link below. / Pour consulter la version de l'éditeur, utilisez le lien DOI ci-dessous.

Publisher's version / Version de l'éditeur:

<https://doi.org/10.1021/la103070x>

Langmuir, 26, 22, pp. 17558-17567, 2010-09-29

NRC Publications Record / Notice d'Archives des publications de CNRC:

<https://nrc-publications.canada.ca/eng/view/object/?id=c66f0770-01a0-4f98-9695-65aa3b0a2be2>

<https://publications-cnrc.canada.ca/fra/voir/objet/?id=c66f0770-01a0-4f98-9695-65aa3b0a2be2>

Access and use of this website and the material on it are subject to the Terms and Conditions set forth at

<https://nrc-publications.canada.ca/eng/copyright>

READ THESE TERMS AND CONDITIONS CAREFULLY BEFORE USING THIS WEBSITE.

L'accès à ce site Web et l'utilisation de son contenu sont assujettis aux conditions présentées dans le site

<https://publications-cnrc.canada.ca/fra/droits>

LISEZ CES CONDITIONS ATTENTIVEMENT AVANT D'UTILISER CE SITE WEB.

Questions? Contact the NRC Publications Archive team at

PublicationsArchive-ArchivesPublications@nrc-cnrc.gc.ca. If you wish to email the authors directly, please see the first page of the publication for their contact information.

Vous avez des questions? Nous pouvons vous aider. Pour communiquer directement avec un auteur, consultez la première page de la revue dans laquelle son article a été publié afin de trouver ses coordonnées. Si vous n'arrivez pas à les repérer, communiquez avec nous à PublicationsArchive-ArchivesPublications@nrc-cnrc.gc.ca.



National Research
Council Canada

Conseil national de
recherches Canada

Canada

Taking a Little off the Top: Nanorod Array Morphology and Growth Studied by Focused Ion Beam Tomography

Kathleen M. Krause,^{*,†} Douglas W. Vick,[‡] Marek Malac,^{‡,§} and Michael J. Brett^{†,‡}

[†]Electrical and Computer Engineering, University of Alberta, Edmonton, Alberta, Canada T6G 2 V4,

[‡]National Research Council (NRC), National Institute for Nanotechnology (NINT), Edmonton, Alberta, Canada T6G 2M9, and [§]Department of Physics, University of Alberta, Edmonton, Alberta, Canada T6G 2G7

Received August 2, 2010. Revised Manuscript Received September 10, 2010

The high surface area, large aspect ratio, and porous nature of nanorod arrays make them excellent foundation materials for many devices. Of the many synthesis techniques for forming nanorods, glancing angle deposition (GLAD) offers one of the more straightforward and flexible methods for ensuring control of alignment, porosity, and architecture of the nanorods. Here we demonstrate the first use of a dual-beam (focused ion beam (FIB) combined with scanning electron microscopy (SEM)) instrument to section and image the internal morphology of a nanorod array fabricated using the GLAD technique. We have used the FIB-SEM to reconstruct the 3D composition of TiO₂ nanorods, allowing us to visualize for the first time the core structures of many potential devices. We have also been able to probe the relationship between critical parameters such as diameter (\bar{w}_{act}), internanorod spacing (\bar{v}_{act}), center-to-center spacing (\bar{c}_{act}), and nanorod population density (d_{act}) and the depth of the nanocolumn (t) for a single homogeneous structure. A continuous data set was obtained from a single 5- μm -thick GLAD film, avoiding the artifacts arising from the analysis of the top surfaces of multiple samples of varying thicknesses. An analysis of the acquired sectioned data has allowed us to determine that the critical nanocolumn parameters follow a power-law scaling trend with $\bar{w}_{\text{act}} = 9.4t^{0.35}$ nm, $\bar{v}_{\text{act}} = 15.2t^{0.25}$ nm, $\bar{c}_{\text{act}} = 24.8t^{0.31}$ nm, and $d_{\text{act}} = 3402t^{-0.65}$ columns μm^{-2} . Using the FIB/SEM images acquired for the TiO₂ nanorods, we have also investigated the evolution of individual nanocolumns and have observed that bifurcation and branching play a significant role in the extinction or survival of these nanorods. These findings will allow for the optimization of nanorod properties for device applications. Also, the FIB sectioning and reconstruction process developed here will permit for the investigation of nanorod arrays formed from a range of synthesis techniques and materials.

Introduction

Surfaces coated in nanowires, nanotubes, and nanorods feature prominently in technologies such as gas sensors, photovoltaic cells, and catalytic surfaces, where the high surface area of these coatings is critical to the device efficiency and sensitivity.^{1–3} Furthermore, control of morphology ensures that applications that require structural support or regularity of the nanoscale framework make arrays of nanorods that are greatly desired. Because of the ease with which arrayed nanorods of a huge range of morphologies are fabricated from a wide variety of materials, the glancing angle deposition (GLAD) technique represents one promising avenue for the production of nanobased devices.^{4–6} However, without a knowledge of the exact nanorod structure or of the nanorod growth processes and competition, device optimization is either difficult or hit and miss. Our application of a dual beam (focused ion beam (FIB) and scanning electron microscopy (SEM)) instrument to segment and then reconstruct a GLAD nanorod array has allowed us to analyze and understand the growth dynamics and morphological characteristics better.

GLAD thin films of nanorods typically exhibit columnar structures with morphology that is determined in part by the source material and in part by the deposition conditions. Through oblique deposition and controlled substrate rotation, this physical vapor

deposition process enables the fabrication of columnar nanostructured films that have been employed in applications from gas sensing to photonics and microfluidics.^{7–9} Understanding how these films grow and the characteristics of their columnar structure is therefore essential not only for optimizing the technique itself but also for advancing the consequent applications.

Important properties of GLAD nanorod arrays, such as their high surface area and column roughness, have been investigated by various groups using gas adsorption porosimetry and transmission electron microscopy (TEM) studies.^{10–14} Other groups have used atomic force microscopy (AFM) to image the tips of GLAD nanorods to measure parameters associated with roughness.¹⁵ Optical ellipsometry and scanning electron microscopy (SEM) are often used to investigate the morphological properties of these films such as their height, width, and density as a function of nanorod height.⁵ Each of these approaches has yielded important information about GLAD nanorod structure; however, each has its limitations, and the recovery of the 3D structure of the film is challenging. SEM imaging offers significant depth of focus,

*Corresponding author. E-mail: katiek@ualberta.ca.

(1) Rajesh, T.; Kumar, D. *Sens. Actuators, B* **2009**, *136*, 275–286.

(2) Boucle, J.; Ravirajan, P.; Nelson, J. J. *Mater. Chem.* **2007**, *17*, 3141–3153.

(3) Guizzard, C.; Princivalle, A. *Catal. Today* **2009**, *146*, 367–377.

(4) Robbie, K.; Brett, M. J. *J. Vac. Sci. Technol., A* **1997**, *15*, 1460–1465.

(5) Hawkeye, M. M.; Brett, M. J. *J. Vac. Sci. Technol., A* **2007**, *25*, 1317–1335.

(6) Lakhtakia, A.; Messier, R. *Sculptured Thin Films: Nanoengineered Morphology and Optics*; SPIE Press: Bellingham, WA, 2004.

(7) Steele, J. J.; Taschuk, M. T.; Brett, M. J. *IEEE Sens. J.* **2008**, *8*, 1422–1429.

(8) Xi, J.-Q.; Schubert, M. F.; Kim, J. K.; Schubert, E. F.; Chen, M.; Lin, S.-Y.; Liu, W.; Smart, J. A. *Nat. Phot.* **2007**, *1*, 176–179.

(9) Bezuidenhout, L. W.; Brett, M. J. *J. Chromatogr., A* **2008**, *1183*, 179–185.

(10) Krause, K. M.; Taschuk, M. T.; Harris, K. D.; Rider, D. A.; Wakefield, N. G.; Sit, J. C.; Buriak, J. M.; Thommes, M.; Brett, M. J. *Langmuir* **2010**, *26*, 4368–4376.

(11) Flaherty, D. W.; Hahn, N. T.; Ferrer, D.; Engstrom, T. R.; Tanaka, P. L.; Mullins, C. B. *J. Phys. Chem. C* **2009**, *113*, 12742–12752.

(12) Demirel, M. C. *Colloids Surf., A* **2008**, *321*, 121–124.

(13) Dohnalek, Z.; Kimmel, G. A.; McCready, D. E.; Young, J. S.; Dohnalkova, A.; Smith, R. S.; Kay, B. D. *J. Phys. Chem. B* **2002**, *106*, 3526–3529.

(14) Malac, M.; Egerton, R. F. *J. Vac. Sci. Technol., A* **2001**, *19*, 158–166.

(15) Vick, D.; Smy, T.; Brett, M. J. *J. Mater. Res.* **2002**, *17*, 2904–2911.

resulting in electron signal detection with a significant component that originates from the interior volume rather than the thin surface layer of the film. AFM images are subject to distortion because of the interaction of the probe with the sample as well as the finite size of the probe. The accuracy of porosimetry is limited by assumptions that must be made about the characteristics of the gas adsorbate and its interactions with the surface. Use of the TEM allows for individual nanorods to be imaged with subnanometer resolution, but the spatial relationships between individual nanorods are not preserved and measurements such as column spacing as a function of column height are not possible. A technique that provides a full 3D view of the columnar structure is therefore required.

A method to probe the full 3D properties of GLAD nanorod arrays would be useful for analyzing one of the most important parameters associated with basic structural characterization: the growth scaling of the column diameter, spacing, and density as a function of film thickness. The growth scaling of these GLAD films has been investigated by a number of groups, with the outcome that the evolution of the columnar cross-sectional diameter ($w(t)$) at a given height (t) above the substrate is described by the following power law:

$$w(t) = w_0 t^p \quad (1)$$

Here, p is the characteristic growth parameter and w_0 is an empirical material-dependent constant.^{16–20} The investigation of this parameter has required the growth of multiple GLAD films, each of a different thickness, in order to determine the dependence of the scaling relationship on nanorod height.

Depending on the material and deposition conditions, GLAD nanorods also exhibit another important property—bifurcation—which is manifested as a single nanorod gradually splitting into two or more individual columnar structures as film growth proceeds. Several researchers have investigated branching and bifurcation in these structures.^{21,22} One of their interesting findings is that the number of branches per column evolves with film thickness. This compliments the shadowing competition that occurs between adjacent nanorods and suggests some competition between branches within one column or between a given branch on a column and the neighboring column. Understanding and controlling bifurcation is essential to the fabrication of uniform structures of consistent architecture and pore size distribution, for example, in photonic crystal and optical filtering applications where the uniformity of the nanorods greatly impacts the optical performance.²³

To further the understanding of the 3D characteristics of GLAD nanorods, including their growth scaling and bifurcation behavior, we have therefore employed the imaging and sectioning capabilities of a dual-beam (FIB-SEM) instrument combined with tomographic reconstruction techniques. FIB tomography involves the serial slicing and imaging of parallel surfaces of a

selected volume, followed by the 3D reconstruction of the volume features.^{24–27} In each slice, the focused ion beam removes a thin layer of material of fixed thickness that is adjustable down to a few nanometers, allowing for detailed analysis of samples. The imaging signal results from either ion-induced secondary electrons or secondary electrons produced by the electron beam of the dual-beam instrument. In either case, the conditions can be adjusted such that only a few nanometers thick layer exposed by FIB milling of the sample contributes to the signal.²⁴ FIB instruments have been used to analyze microstructures and buried features, perform crack analysis, and analyze the nanostructure of composite materials.^{27–30}

Here we have concentrated on GLAD nanorod arrays that have been fabricated from titanium oxide (titania, TiO_2). Titania is a material of interest in a variety of processes because its crystal structure can be controlled by deposition conditions and thermal annealing; it forms a noncrystalline thin film when deposited at low temperature but can form crystalline phases such as anatase or rutile when annealed at high temperature.³¹ TiO_2 was also chosen because of its wide use in a number of applications. For example, the combination of its high refractive index and control over the GLAD columnar morphology make titania an excellent material for photonic devices.^{5,6} Humidity sensors are constructed from titania because of its hydrophilicity and stability.⁷ TiO_2 is also a photocatalyst and is therefore used for a number of environmental sensing, photovoltaic, and purification applications.^{32,33}

In this article, we describe our development of an FIB-SEM tomography technique for the sectioning and 3D reconstruction of arrays of nanorods. Furthermore, we have investigated the growth scaling and bifurcation characteristics of a representative metal oxide GLAD nanostructured thin film. Individual nanorods within the volume have been isolated through new sectioning and imaging routines such that bifurcation and scaling behavior could be tracked. To our knowledge, this is the first direct investigation of properties of a single nanorod as a function of thickness. These findings should enable improved optimization and understanding of the growth of GLAD nanostructures. They will also provide details of the tomography technique that will allow the study and improvement of various nanoscale architectures of materials fabricated by GLAD and other processes.

Materials and Methods

Several steps were required to prepare the specimens for tomography. The first was to deposit an amorphous 5080 ± 10 nm TiO_2 (material source, Cerac; 99.9% pure rutile) vertical nanorod film by electron-beam physical vapor deposition evaporation (Axxis, Kurt J. Lesker). The film was deposited at a vapor angle of incidence of 85° with continuous substrate rotation. The heating of the oxide by the electron beam results in a gradual depletion of oxygen content in the evaporant; stoichiometric TiO_2 was ensured by the introduction of O_2 gas flow to maintain a deposition pressure

(16) Taschuk, M. T.; Krause, K. M.; Steele, J. J.; Summers, M. A.; Brett, M. J. *J. Vac. Sci. Technol., B* **2009**, *27*, 2106–2111.

(17) Mukherjee, S.; Gall, D. *Appl. Phys. Lett.* **2009**, *9*, 173106.

(18) Kaminska, K.; Amassian, A.; Martinu, L.; Robbie, K. J. *Appl. Phys.* **2005**, *97*, 013511.

(19) Karabacak, T.; Singh, J. P.; Zhao, Y.-P.; Wang, G.-C.; Lu, T.-M. *Phys. Rev. B* **2003**, *68*, 125408.

(20) Buzea, C.; Beydaghyyan, G.; Elliot, C.; Robbie, K. *Nanotechnology* **2005**, *16*, 1986–1922.

(21) Wang, J.; Huang, H.; Kesapragada, S. V.; Gall, D. *Nano Lett.* **2005**, *5*, 2505–2508.

(22) Zhou, C. M.; Gall, D. *Appl. Phys. Lett.* **2006**, *88*, 203177.

(23) Summers, M. A.; Brett, M. J. *Nanotechnology* **2008**, *19*, 415203.

(24) Sakamoto, T.; Cheng, Z.; Takahashi, M.; Owari, M.; Nihei, Y. *Jpn. J. Phys.* **1998**, *37*, 2051–2056.

(25) Kubis, A. J.; Shiflet, G. J.; Dunn, D. N.; Hull, R. *Metall. Mater. Trans. A* **2004**, *35*, 1935–1943.

(26) Munroe, P. R. *Mater. Char.* **2009**, *60*, 2–13.

(27) Groeber, M. A.; Haley, B. K.; Uchic, M. D.; Dimiduk, D. M.; Ghosh, S. *Mater. Char.* **2006**, *57*, 259–273.

(28) Kubis, A. J.; Vandervelde, T. E.; Bean, J. C.; Dunn, D. N.; Hull, R. *Appl. Phys. Lett.* **2006**, *88*, 263103.

(29) Holzapfel, C.; Schaf, W.; Marx, M.; Vehoff, H.; Mucklich, F. *Scr. Mater.* **2007**, *56*, 697–700.

(30) Lowell, S.; Shields, J. E.; Thomas, M. A.; Thommes, M. *Characterization of Porous Solids and Powders: Surface Area, Pore Size and Density*; Springer: Dordrecht, The Netherlands, 2006.

(31) Colgan, M. J.; Djufors, B.; Ivey, D. G.; Brett, M. J. *Thin Solid Films* **2004**, *466*, 92–96.

(32) Fujishima, A.; Rao, T. N.; Tryk, D. A. *J. Photochem. Photobiol. C* **2000**, *1*, 1–21.

(33) Taschuk, M. T.; Steele, J. J.; van Popta, A. C.; Brett, M. J. *Sens. Actuators B* **2008**, *134*, 666–671.

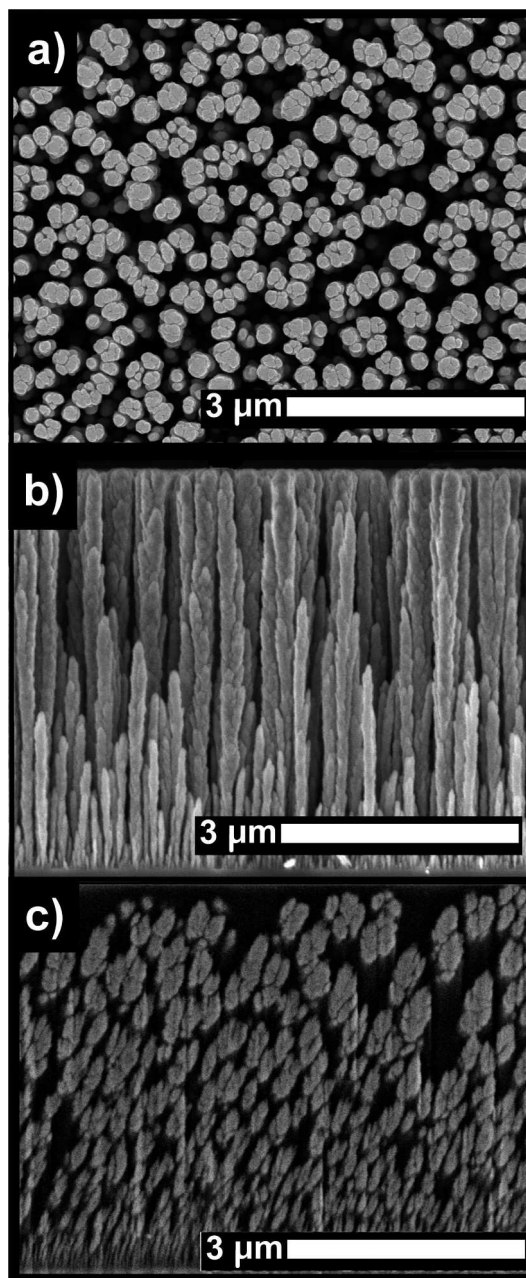


Figure 1. (a) Top-down and (b) side-view cross sections of an original $5\ \mu\text{m}$ TiO_2 GLAD nanorod thin film deposited at $\alpha = 85^\circ$. (c) Side-view FIB-sliced cross section of the polymer-filled film.

of 7×10^{-5} Torr, followed by postdeposition annealing in air at $150\ ^\circ\text{C}$ for 24 h.^{34,35} During the deposition, we achieved a typical deposition rate onto the film substrate of $5\ \text{\AA}\ \text{s}^{-1}$. Following deposition, the porous structure was filled with a polymer-based photoresist (HPR504, Arch Chemicals) using a standard spin-in process repeated twice to ensure photoresist infiltration: (i) 500 rpm spin for 10 s, (ii) 3000 rpm spin for 40 s, and (iii) a soft bake at $115\ ^\circ\text{C}$ for 90 s. This filling was performed to ensure that during FIB slicing only the exposed surface would be imaged, with no columnar features from further into the film being captured. The sample was imaged before and after polymer filling by a Hitachi cold field emission S-4800 SEM, as shown in Figure 1. An artifact of the filling process is that the nanorods become slightly inclined. This is likely due to the spinning step or to internal stresses during curing.

The resultant inclination angle for the present sample was approximately 10° , reducing the film thickness to $5000 \pm 30\ \text{nm}$.

In preparation for tomography, a twice-filled GLAD sample was cleaved from the wafer substrate, coated with a thin (20 nm) coating of gold to ensure good conductivity, and mounted onto specimen holders with an inclined mounting surface using heat-bondable silver epoxy. The sample was then mounted onto the six-axis FIB stage of a Zeiss NVision 40 Crossbeam Workstation, which features a vertically aligned SEM column and an FIB column oriented at 54° with respect to the vertical. Microscopy was performed at the edge of the sample; the inclined orientation of the sample allowed edge milling to be performed from two orthogonal directions, as described below.

The sample was first oriented such that the FIB probe was normal to the wafer substrate, as shown in Figure 2a,b. A high current probe FIB probe was used to mill into the sample edge approximately $5\ \mu\text{m}$, exposing a fresh surface of the sample and removing any edge defects introduced during the cleaving step. The exposure typically extended $50\ \mu\text{m}$ along the sample edge and at least $10\ \mu\text{m}$ deep. The SEM was then used to select an appropriate site for the tomography step. This portion of the exposure was then subjected to a sequence of polishing steps using FIB probe currents from 3 nA down to 150 pA. The objective of this step was to planarize the edge by removing as much as possible the curtaining effects that resulted from the different milling rates of the TiO_2 and photoresist.

In the final step prior to serial slicing, the sample was returned to the first orientation and ion-beam-assisted deposition was used to create a protective layer of carbon on the surface that was polished in the previous step. A phenanthrene precursor was introduced onto the sample surface using a gas injection system and dissociated by the 300 pA FIB probe and by locally generated secondary electrons, thereby producing a carbon layer of approximately $1\ \mu\text{m}$ thickness.

During the FIB tomography stage, serial slicing progressed from the photoresist capping layer through the nanorod film and toward the silicon substrate, exposing surfaces parallel to the substrate plane, as shown in Figure 2c,d. After each slice was milled, an SEM image was acquired with the in-lens detector and an electron beam energy of 3.0 keV. The SEM images were scanned at a resolution of 2048 pixels \times 1536 pixels, with tilt-correction enabled in the NVision software to compensate for foreshortening such that the pixel sizes in the x and y directions were identical. An image subdomain with typical dimensions of 1000 pixels \times 1000 pixels was selected from the original image for tomographic reconstruction and morphological analysis. During the milling procedure, the FIB and SEM magnifications were locked and the FIB imaging/milling resolution set to 512 pixels \times 384 pixels. Consequently, the volume elements of the reconstructed image series were not cubes but rectangular elements with dimensions of $1 \times 1 \times 4$ (width \times length \times height). A 300 pA milling probe was used for the first two slice series, and a 150 pA probe was used for the remaining high-resolution series. The probe spots contained 50% of the beam energy within diameters of 38 and 29 nm, respectively. The choice of probes ensured that the pixel fill factor during milling exceeded 100%, in accordance with standard milling practice.

The NVision GUI allowed us to automate the milling procedure after appropriate focal, scanning, and detector settings were selected. Because of the inherent scaling of the film (with column diameters growing larger as one progresses from the substrate–film interface toward the top of the film), the slicing was broken into several slice sequences, using progressively higher magnification, smaller fields of view and smaller milling volumes for each successive layer. The FIB was instructed to mill a trapezoidal volume for each slice series (i.e., a wider milling surface was used at the beginning of the given slice series than at its end in order to allow for redeposition of milled material to occur without impacting the milled volume side walls). The multiple slice sequences also helped to manage stage, sample, and probe drift by realigning the sample at the beginning of each sequence. The typical

(34) Rao, K. N. *Opt. Eng.* **2002**, *41*, 2357–2364.

(35) Wang, W.-H.; Chao, S. *Opt. Lett.* **1998**, *23*, 1417–1419.

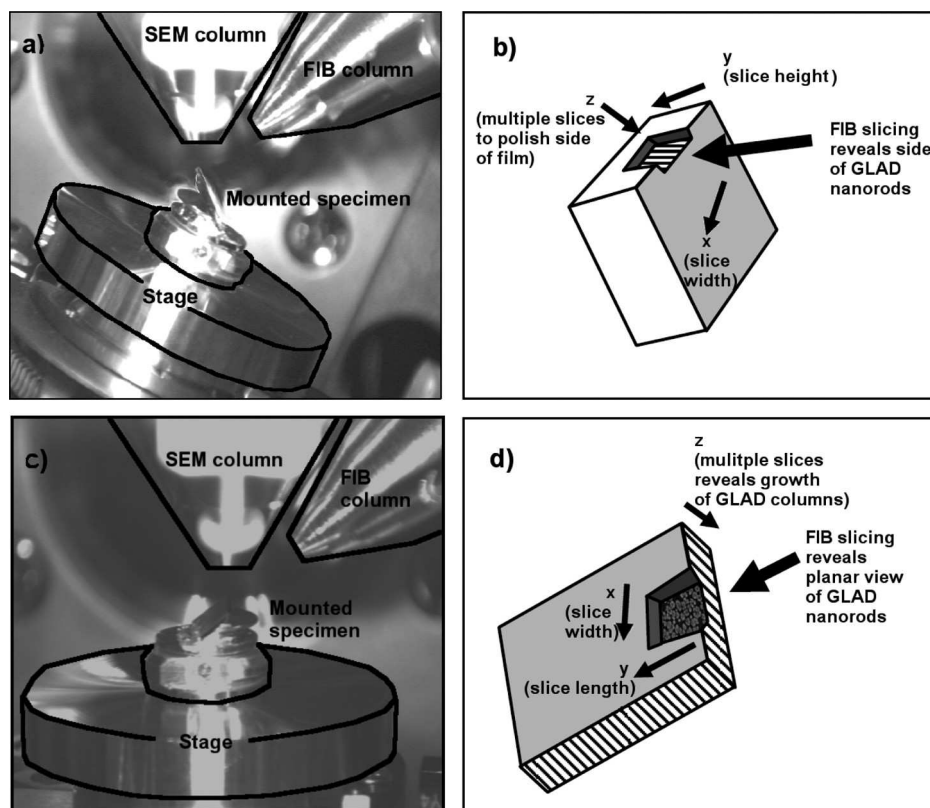


Figure 2. (a) Specimen orientation relative to FIB and SEM columns for the side-polishing procedure. (b) Side-polishing schematic. (c) Specimen orientation relative to FIB and SEM columns for the tomographic slicing process. (d) Tomographic slicing proceeds from the top of the film toward the substrate, exposing a planar cross section of the GLAD film.

slice sequence involved the execution of roughly 100 slice and image captures. SEM magnification settings were chosen such that the pixel size and slice thickness of the initial sequence were 4.0 and 16.0 nm, respectively. For the final sequence, the corresponding dimensions were 1.0 and 4.0 nm. The cross-sectional area was constant for all slices in a given series but decreased from $15.0 \mu\text{m}^2$ for the first series to $0.14 \mu\text{m}^2$ for the last. The total volume analyzed was approximately $30 \mu\text{m}^3$.

Once the complete set of the slice series was acquired, the images were postprocessed in preparation for 3D reconstruction and tomographic analysis. Postprocessing, with custom MATLAB software routines, involved image registration and alignment to compensate for image drift. To accomplish this, a rectangular fiducial region, unmilled during serial slicing and common to all images with a given slice series, was used to align the images. The drift of this fiducial frame was tracked through the image sequence using a routine that minimized the sum of the squared differences in pixel values between the detected fiducial region in a given image and the fiducial region in the first image. An additional translation of the frame in the positive y direction was required to compensate for the advancement of the milling surface into the sample. In principle, the required shift was known precisely from the milling recipe. In practice, an additional alignment check was performed. Here, we made use of the contrast step across the interface between the sample and the protective carbon layer. Total shifts in the row and column directions were typically several hundred pixels, translating into several hundred nanometers to micrometers of spatial shift.

For each image, local charging and other artifacts were compensated for through a custom equalization routine similar to adaptive histogram-based equalization algorithms implemented in MATLAB and other groups.³⁶ To accomplish this, the image was broken into a grid of $n \times n$ tiles (typically $n = 2$ or 3).

(36) Zuiderveld, K. Contrast Limited Adaptive Histogram Equalization. *Graphic Gems IV*; Academic Press: San Diego, 1994.

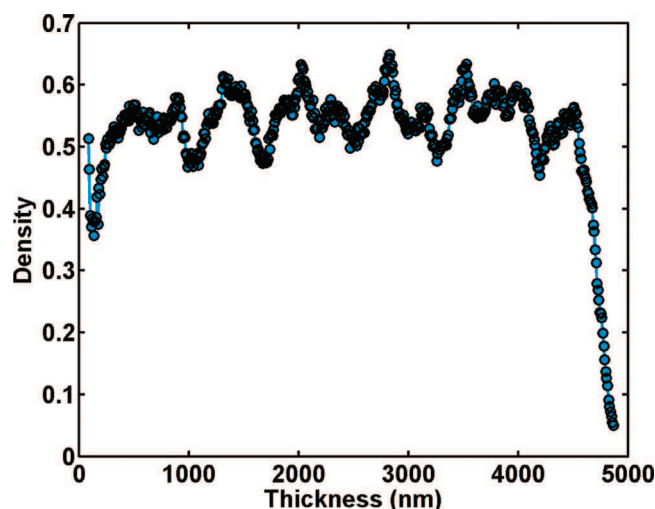


Figure 3. Material density profile of the GLAD nanorod film as extracted from Figure 1c.

The multiplication matrix required to achieve a target image-average histogram for the grayscale pixels within each grid tile was then calculated. This multiplication matrix was then compiled for the entire image, filtered in both dimensions with a moving average filter of length that is half that of the tile size to ensure no discontinuities across tile boundaries, and then applied to the original image. From image to image, contrast differences were compensated for by normalizing the image average density. Images were thresholded to achieve the average density profile described in Figure 3 and are discussed in the following section.

To reconstruct a larger volume of the GLAD film than that covered by just one slice series, several slice series layers had to be

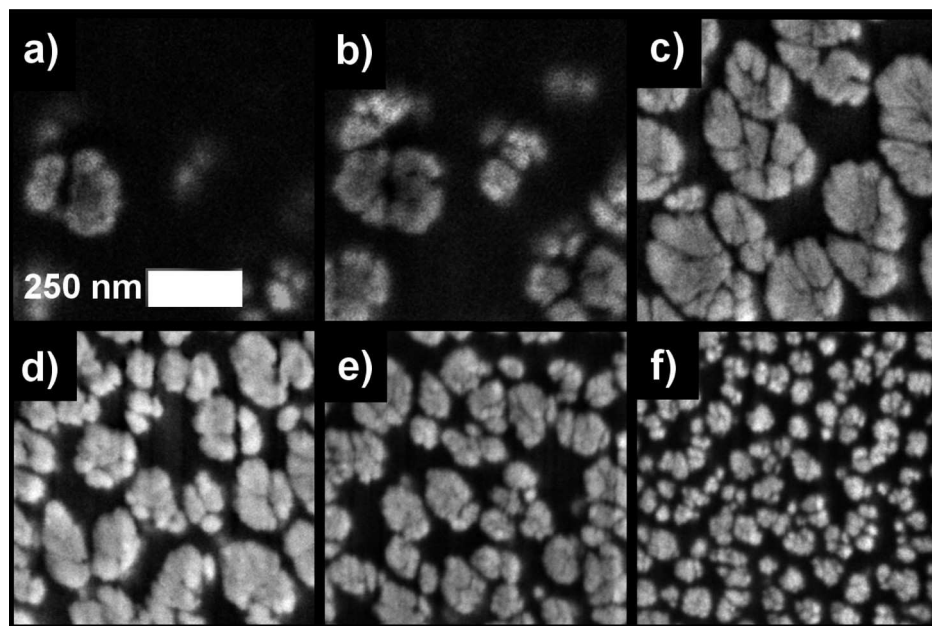


Figure 4. Top-down FIB cross sections of the $5\ \mu\text{m}$ GLAD nanorod array film (a) 4390, (b) 4240, (c) 3360, (d) 1770, (e) 1220, and (f) 980 nm above the substrate. These cross sections illustrate the evolution of nanorod diameter, spacing, and density.

stitched together. To tackle differences in alignment from series to series, stitching was carried out by correlating similar features of the last image of a given slice series to those in the first image of the next series using a summed square pixel difference minimization technique similar to that used for image registration. The stitching of consecutive series was carried out from the substrate toward the top of the film. This was done because the slices further into the film were captured at a higher magnification and a lower absolute area: this magnification and the selected region of interest dimensions at the bottom of the film had to be carried through for all images in the stitched series. A consequence of this is that 2D image interpolation had to be carried out for lower-magnification slices. This interpolation entailed using the MATLAB *imresize* function to interpolate all images from each of the slicing series to the same grid size and resolution. Once stitched together, a large 3D volume of a GLAD film, consisting of equal side grayscale voxels, could be reconstructed. This reconstruction was performed by stacking together the 2D images. Because the slicing resolution was different for each of the series, multiple copies of slices were stacked together to achieve uniform scaling within the reconstructed volume.

Results and Discussion

The development of a process to section, image, and reconstruct an obliquely deposited film through dual FIB-SEM tomography was carried out on the $5\ \mu\text{m}$ columnar TiO_2 GLAD nanorod array shown in Figure 1. We assessed the material density (a fraction of the bulk density), nanorod density (i.e., number of nanorods per area), growth scaling, and bifurcation properties of the nanocolumns using the 3D data set that had been acquired through FIB sectioning. For example, the side-milled view of the thin film specimen was used to determine the material density profile for the film. The origin of the slight nanorod tilt is explained later. The material density profile is shown in Figure 3 and is quasi-stable as a function of film thickness, with the oscillations that are observed consistent with simulation work described in the literature.³⁷ These oscillations may be a consequence of self-shadowing competition

between the nanocolumns; columns grow large until periodically a certain percentage die out at the expense of others. Toward the substrate, the density appears to decrease, although image resolution makes it difficult to determine the density of the film nucleation region precisely.

Once acquired, the top-down milled cross sections of the GLAD nanorod array were used for tomographic reconstruction and analysis. Seven series of SEM images, each set taken at progressively deeper depths into the film and each consisting of multiple consecutive SEM cross-sectional views, were produced. The growth scaling characteristics of the investigated FIB sliced array were then found by studying each SEM image from each slice series. As described in the Materials and Methods section, the preparation of the GLAD film for FIB tomography resulted in an imposed tilt on the nanorods of the film, as can be observed in Figure 1c. We did not attempt to recover the original vertical orientation of the nanorods; consequently, the reconstructions exhibited the tilted structures in correspondence with the filled heterogeneous specimens.

Representative cross sections of the GLAD nanorod array are shown in Figure 4. Toward the substrate, the film is composed of a large number of small, closely spaced nanorods that are tens of nanometers wide. This is the region where initial nucleations of deposited material become the first GLAD nanorods. Some of these become extinct through competitive growth processes, and as we move upward toward the top of the film, the rods broaden and the average spacing between the nanorod centers increases. After several micrometers of film deposition, the rod diameters reach several hundred nanometers. At the very top of the film, shown in Figure 4a, only the tips of the tallest rods can be seen when a cross-sectional FIB slice is taken.

Figure 4 also illustrates that it is difficult to determine the exact point at which nanorods emerge from the polymer matrix and manifest their presence fully. One can see that over a slicing depth of 150 nm, in Figure 4a,b, the hints of the very tips of the nanorods evolve to reveal full columnar cross sections, but it is difficult to determine the point at which the tips of the nanorods fully appear. We estimate that electrons probing the surface reveal features via detection of backscattered electrons (BSEs) to a depth

(37) Smy, T.; Vick, D.; Brett, M. J.; Dew, S. K.; Wu, A. T.; Sit, J. C.; Harris, K.D.. *J. Vac. Sci. Technol., A* **2000**, *18*, 2507–2512.

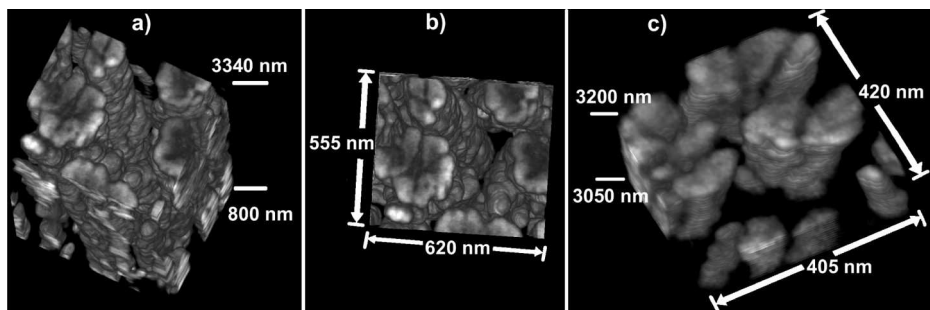


Figure 5. Three-dimensional tomographic views of a stitched GLAD film showing (a) a representative volume at an oblique angle such that columnar features are visible and (b) a view from the top of image a down through the film. (c) An extracted volume where surface details are visible on the individual nanorods.

of approximately 80 nm into the photoresist matrix.³⁸ However, because we used an in-lens detector, secondary electrons (SEs) dominate the detected signal. Surface features and the atomic number contrast are therefore the principal characteristics imaged. This means that their interaction with still-buried TiO₂ rods is likely on the order of several tens of nanometers.

Once images from consecutive slice series were stitched together into a single data cube, a reconstructed volume was created. This 3D data cube was imported into the JEOL TEMography Visualizer software (v 2.2, 2006) for imaging. This program allowed for the volume to be viewed, rotated, and magnified while parameters such as opacity and contrast were controlled. Representative 3D reconstructions of a GLAD columnar array are shown in Figure 5. Images a and b are different views of the same volume. They show that the features of individual nanorods are apparent, as is the relationship between adjacent nanorods. Image c reveals details of a magnified region of this volume. Discrete slices are visible in this image, as are some details of the surface of the GLAD nanorods. The nanorods can be seen to be rough and made up of clumps of bifurcated arms, verifying previous reports from 2D SEM data that GLAD films appear to bifurcate as they grow.^{21,22}

To assess the growth scaling property of the GLAD film being analyzed, the sectioned slice images were assessed as a function of the height of the film from the substrate using a custom grain-detection algorithm. Grain-detection algorithms, which identify individual nanorods, have been used by other groups to analyze the top-down SEM images produced for GLAD films.^{20,39} Our grain-detection algorithm first required the identification of connected regions of each equalized and thresholded SEM cross section such as that shown in Figure 6 a,b. Equalization was used to normalize the contrast within a given image as well as to ensure uniform contrast from image to image. This uniform contrast was achieved by adjusting the grayscale threshold value to achieve a constant density equal to the average found in the side-view analysis shown in Figure 3. Because the precise location above the substrate–film interface was not known, we did not attempt to match the oscillatory nature of the actual density profile. Identification of individual nanorods and connected regions of nanorods was done using the MATLAB bwlable routine. The individual nanorods and connected regions of a representative cross-sectional slice of the GLAD film are shown in Figure 6d. The connected regions were broken into individual columns through a custom algorithm that found and broke small concave bridges within connected domains, as illustrated in Figure 6e.

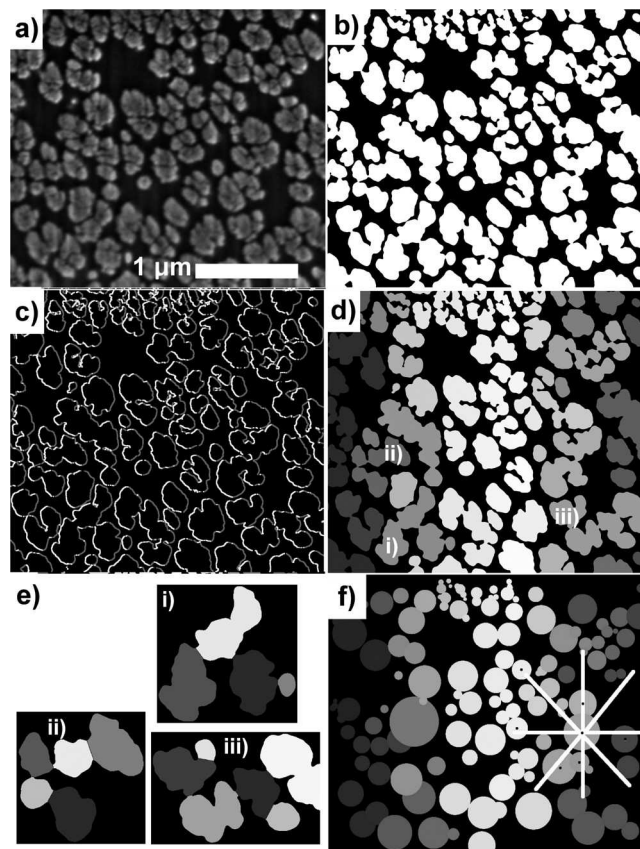


Figure 6. (a) Equalized top-down cross section of an FIB-sliced GLAD film in the second series (4240 nm from substrate), (b) thresholded image, (c) edge image showing the transitions from the void to the nanorod (white line) and from the nanorod to the void (gray line), (d) connected nanorods identified by unique color, (e) individual nanorods identified with connected regions, and (f) nearest-neighbor identification.

Once nanorods had been classified, the column density per slice image was estimated by counting the number of nanorods per cross-sectional image area. The nearest neighbors of each nanorod within each image were also identified along trajectories at 30° increments as illustrated in Figure 6f. The mean distance to the nearest neighbor of each nanorod within each slice was calculated. Nanorods that bordered the edge of the image were excluded from this analysis. Finally, the overall mean nanorod diameter and nanorod center-to-center spacing were calculated for each image slice.

To determine the average spacing between adjacent nanorods, the length of all void distances between nanorods, along every

(38) Goldstein, J.; Newbury, D.; Joy, D.; Lyman, C.; Echlin, P.; Lifshin, E.; Sawyer, I.; Joseph, M. *Electron Beam-Specimen Interactions. Scanning Electron Microscopy and X-ray Microanalysis*, 3rd ed.; Springer: New York, 2003.

(39) Kaminska, K.; Amassian, A.; Martinu, L.; Robbie, K. J. *Appl. Phys.* **2005**, *97*, 013511.

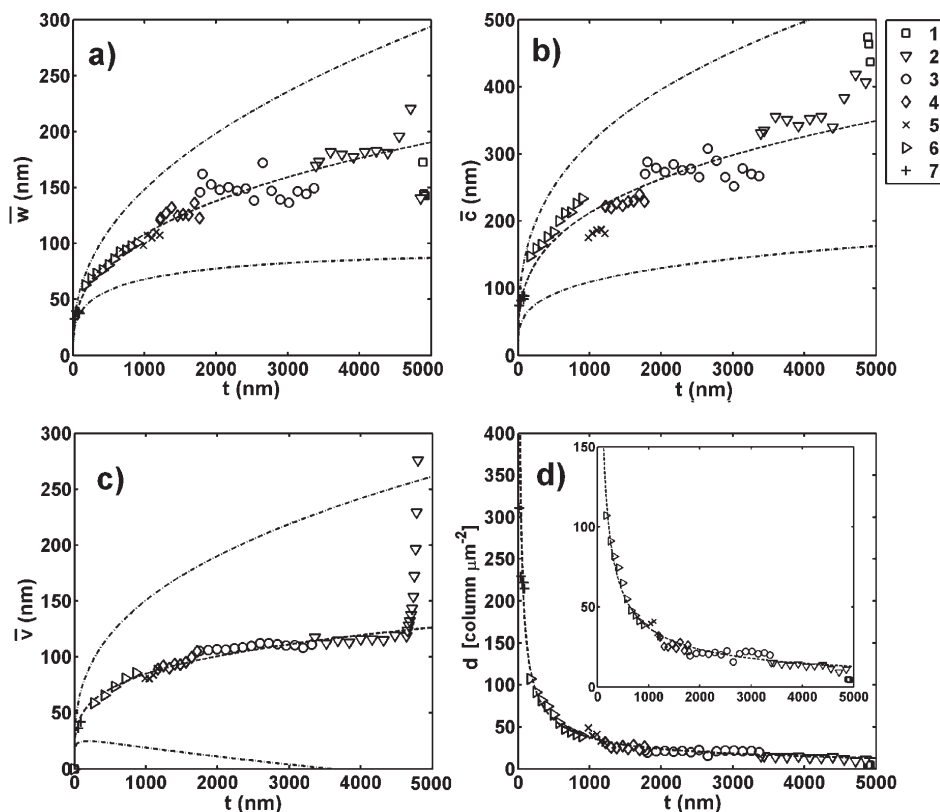


Figure 7. (a) Mean nanorod diameter scales as $\bar{w}_{\text{act}} = 9.5t^{0.35}$ nm ($\bar{w}_{\text{act}} = 9.4t^{0.35}$ when the nanorod tilt is compensated for) where t is in nanometers. (b) Nanorod center-to-center spacing between nanorods scales as $\bar{c} = 25.1t^{0.31}$ nm ($\bar{c}_{\text{act}} = 24.8t^{0.31}$). (c) Void spacing scales as $\bar{v} = 15.4t^{0.25}$ nm ($\bar{v}_{\text{act}} = 15.2t^{0.25}$). (d) Nanorod density scales with thickness $d = 3.4 \times 10^3 t^{-0.65}$ column μm^{-2} . The inset shows a magnified region of the nanorod density plot. The dotted line through the data points shows the scaling fit. Dashed–dotted lines show one standard deviation of parameter distributions.

pixel row and column of each thresholded SEM image, was first found. This was done by calculating the distance between all adjacent nanorod-to-void and void-to-nanorod edges in an edge-detected image such as that shown in Figure 6c. The mean internanorod spacing was then calculated from the distribution of all void spacings in the row and column directions.

The growth scaling parameters of mean nanorod diameter, void spacing, center-to-center spacing, and density are shown in Figure 7. The different symbols shown in these plots represent the separate slice series. Scatter within each slice series and between slice series is due to the sensitivity of the nanorod (grain) detection routines to image contrast nonuniformity, resolution, nearness of adjacent nanorods, and bifurcation characteristics of individual nanorods. Figure 7a illustrates quantitatively the nanorod diameter growth scaling from tens to hundreds of nanometers over a thickness of several micrometers, as observed in Figure 4. This column diameter curve shows the characteristic self-similar scaling seen for GLAD films. An abrupt dip in the mean diameter curve occurs at the maximum film thickness because only the very tips of the tallest columns are imaged at this point. A power law fit to the mean diameter curve reveals a relationship of $\bar{w} = 9.5t^{0.35}$ nm, with t being valid from ~ 100 to ~ 5000 nm. (Data from the very bottom and top of the film were disregarded.) Compensation for the $\theta = 10^\circ$ tilt in the filled film results in a stretching of the thickness axis from a maximum thickness of 5000 to 5080 nm and a reduction in mean width by $(\cos \theta)^{1/2}$ to yield a relationship between the actual diameter (\bar{w}_{act}) and a thickness of $\bar{w}_{\text{act}} = 9.4t^{0.35}$ nm. The lines above and below the data points represent a fit to one standard deviation from the mean of the nanorod diameter distributions. The width of the distributions is of the

same order as that of the mean diameter, indicating a wide range of diameters at every stage of nanorod growth.

The exponential factor of 0.35 describing the growth scaling of the nanorod diameter is in line with the findings of previous groups for metal oxide films, where p values ranging from 0.3 to 0.5 have been found for metal oxide GLAD films deposited at an oblique angle of 85° .¹⁶ It has also been speculated that nanorod growth, which is dominated by shadowing, should result in a p value of 0.5 whereas large adatom diffusion should result in a scaling factor of 0.3.¹⁹ Our scaling factor of 0.35 therefore suggests that adatom diffusion is a significant factor in the growth of TiO_2 films.

The void spacing between nanorods also follows a self-similar growth pattern. Figure 7c reveals a power-law scaling trend of mean void spacing versus a thickness of $\bar{v} = 15.4t^{0.25}$ nm. The tail at 5000 nm is due to the large gaps between the very tips of the tallest nanorods at the top of the film. Compensation for film tilt results in a void spacing relationship of $\bar{v}_{\text{act}} = 15.2t^{0.25}$ nm. Similarly, the columnar nearest-neighbor center-to-center spacing grows with a power-law relationship of $\bar{c} = 25.1t^{0.31}$ nm. This curve is shown in Figure 7b. By compensating for the tilt in the film, the spacing relationship becomes $\bar{c}_{\text{act}} = 24.8t^{0.31}$ nm. Interestingly, it can be seen that the center-to-center and internanorod void spacing grow at rates slower than that of the nanorod diameter. This indicates that whereas the absolute spacing between the nanorods grows and is significant after a thickness of several micrometers, nanorods are becoming relatively closer to each other as they grow. The self-shadowing effect appears to change with increasing film thickness and diameter, being significant for small initial nuclei and the beginnings of nanorods but less so as nanorods grow. This indicates that the growth scaling of

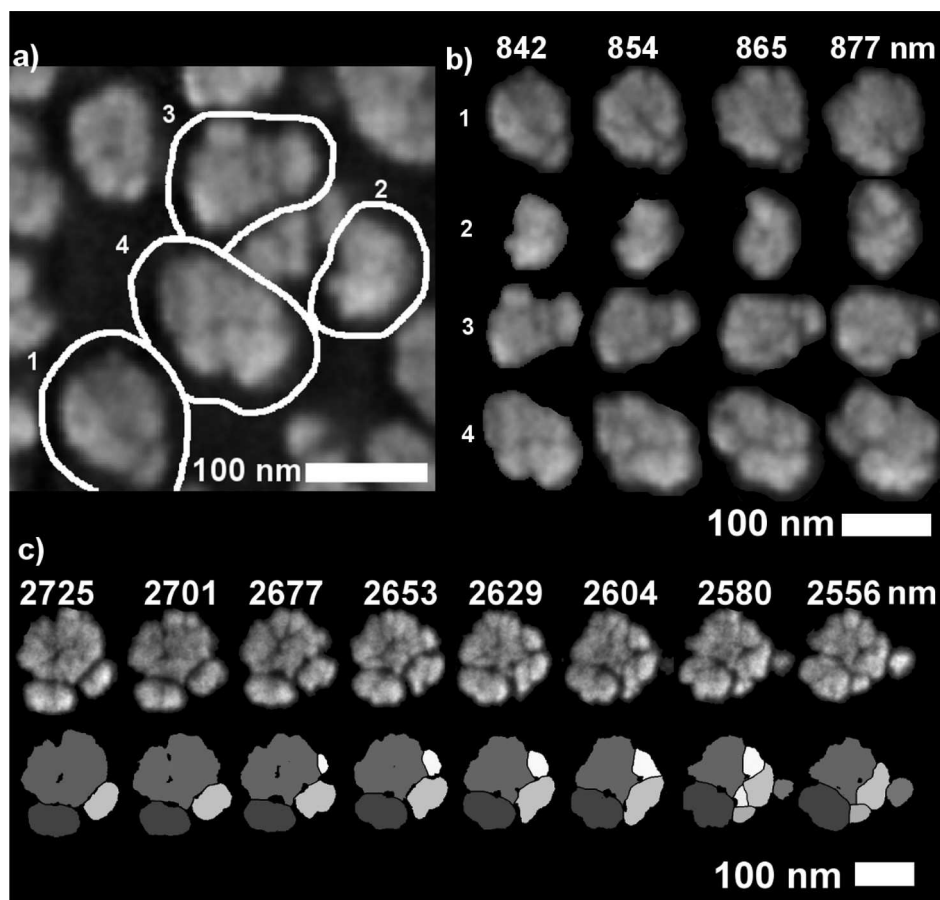


Figure 8. Tracking of four individual nanorods beginning at 842 nm from the substrate. (a) Initial configuration of the nanorods, (b) Evolution of these nanorods through several tens of nanometers, and (c) progress of the evolution of nanocolumn 1 bifurcation from 2556 to 2725 nm.

initially seeded GLAD films may follow a slightly different initial growth trajectory than those that naturally nucleate. The growth scaling properties of both nanorod diameter and spacing will also have to be taken into account for applications employing GLAD structures, such as microfluidic separation devices for which internanorod spacing may be a critical parameter.⁶

The nanorod density is plotted as a function of thickness in Figure 7d. As expected, the density of nanorods per unit area decreases as the nanorods broaden. There are a large number of rods close to the film–substrate interface, but as these nanocolumns grow and compete, only the largest survive. A fit to the trend reveals an inverse power law scaling of $d = 3400t^{-0.65}$ columns μm^{-2} for t from ~ 100 to 5000 nm. Compensation for the actual thickness of the film results in a revised fit of $d_{\text{act}} = 3402t^{-0.65}$ columns μm^{-2} . Because this parameter is cast in terms of area, the inverse doubling of the nanorod diameter power-law exponent is expected because we set the image contrast for each image to achieve a constant pixel density. The rate of density decrease is also as expected from the rate of growth in nanocolumn diameter. As the nanorods grow in size, the number per area will obviously decrease.

To verify that the thickness scaling relationships of the mean columnar width, void spacing, and center-to-center spacing agreed, a quick check was performed. Because the cross-sectional density is roughly constant throughout the thickness of the film (with the exception of the initial growth region and the region at the top of the film), the nanorod center-to-center spacing (\bar{c}_{est}) should be roughly equal to the sum of one nanorod diameter

and the void spacing between nanorods:

$$\bar{c}_{\text{est}} = \bar{w} + \bar{v} \quad (2)$$

The summation of the nanorod diameter and void spacing relationships reveals an expected nanorod center spacing of $\bar{c}_{\text{est}} = 23.3t^{0.31}$ nm, which is close to that determined from Figure 7b.

In addition to calculating average properties for each slice image of the GLAD film, we also tracked several individual nanorods through a portion of the film. These nanorods, identified in the initial slice image shown in Figure 8a, were tracked from slice to slice from 840 to 3080 nm above the substrate toward the top of the film. Because of stage drift, the requirement was to realign the series in between slice series and rod tilt. This is as far as the nanorods could be tracked. Only one nanocolumn (column 1) continues beyond 3080 nm thickness but could not be followed further because it reached the edge of the FIB-polished sample side face.

Tracking of these nanocolumns involved matching column cross sections from image to image using a custom MATLAB routine and the use of the Gimp (GNU image manipulation program, v2.6.8) image processing program. Figure 8b shows how the four tracked rods evolve over the first few slices. To examine the bifurcation of the tracked columns, the branches were identified for each cross-sectional slice of each column. Each columnar cross section was then divided into sections by eye and by using the Gimp software package. Figure 8c illustrates how the branches of one nanocolumn evolve over several hundred nanometers.

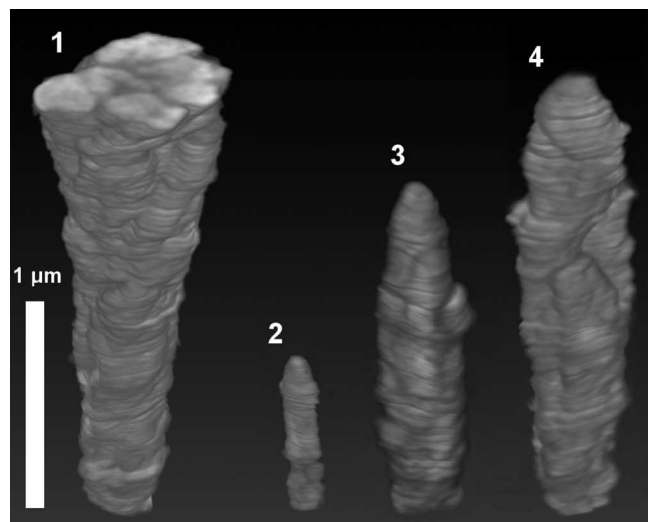


Figure 9. Tomographic view of four individual nanocolumns: from 840 nm to (1) 3080, (2) 1510, (3) 2170, and (4) 2760 nm above substrate.

For each nanorod, the number of branches and arms (B) was tracked as a function of film thickness. The diameter of each of these branches (w_B) was also captured.

Figure 9 shows the 3D reconstructions of these four nanocolumns. The smallest of the columns tracked, column 2, survives only 700 nm from the initial tracking depth. In addition, despite having an initially similar cross-sectional area, columns 3 and 4 die out before column 1, at heights of 2170 and 2760 nm, respectively. Although it was not surprising that a nanorod with a smaller diameter than that of neighboring columns would not persist, the survival of column 1 at the expense of columns 3 and 4 is worth exploring.

To investigate the relative behavior of the four nanocolumns under investigation, several metrics were monitored as a function of column height (t). The diameter (w) of each of these nanorods is plotted in Figure 10a. What is immediately apparent is that the diameter of column 2 rises and modulates for several hundred nanometers and then falls off as the structure disappears. In contrast, for several hundred nanometers the diameters of columns 1, 3, and 4 rise together, with their diameter growing to several hundred nanometers. The diameter of column 3 then levels off and begins to drop. Subsequently, despite following a growth trajectory until 2000 nm, column 4 dies out by 2760 nm. Only column 1 sees its diameter continue to rise without receding. A comparison of Figure 10a with Figure 7a may reveal why either column 1 or 4 survives at the expense of the other. By 2000 nm, columns 1 and 4 both have a diameter of approximately 200 nm. This exceeded the mean diameter expected at this film height. Two neighboring nanorods that exceed the mean diameter predicted by the growth scaling model compete with each other such that one must expire.

A related metric, the cumulative surface area (SA) of each nanorod in a given cross section (i)

$$SA = \sum_i m_i \Delta t_i \quad (3)$$

relative to the footprint area (FA) under the four initial nanorods

$$A = \frac{SA}{FA} \quad (4)$$

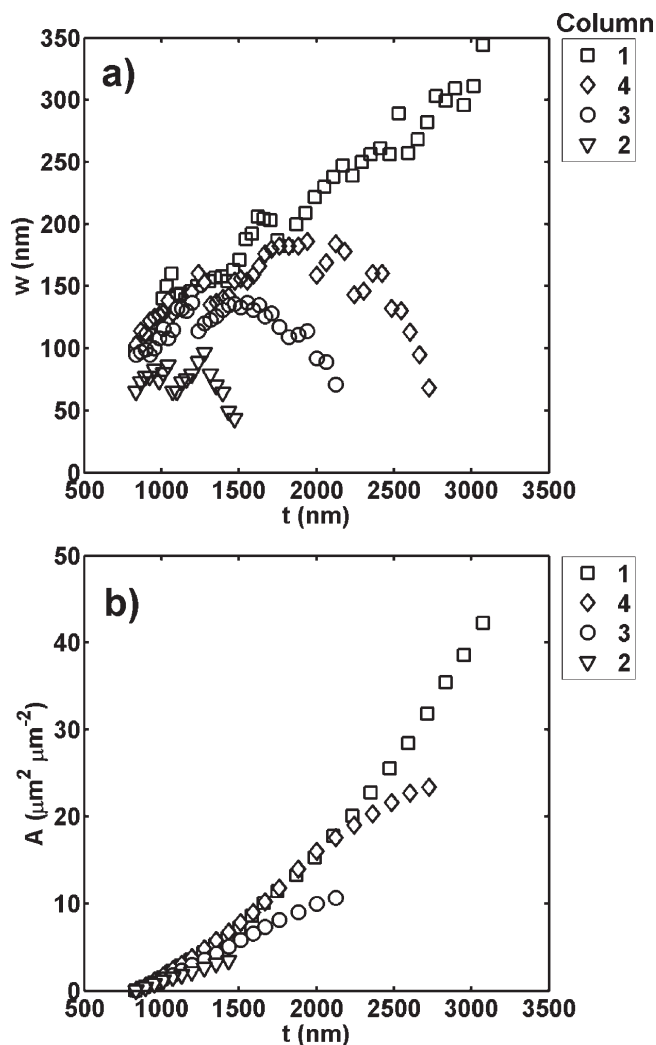


Figure 10. (a) Individual nanorod diameters and (b) cumulative relative surface areas.

where Δt_i is the thickness of the slice, w_i is the column diameter, and m_i is the perimeter circumferential area, is plotted in Figure 10b. This plot reveals that as a nanorod is reaching its height limit the surface area curve inflects and levels off. Interestingly, while the nanorod continues to grow, its surface area rises in a slight superlinear trend.

Finally, Figure 11 shows the number of branches and arms of each individual nanorod as a function of column height. The branches that were tracked are those with a diameter greater than 10 nm. The resolution of the acquired SEM images was not sufficient to study branching and bifurcation on a smaller scale than 10 nm. Further work with the TEM of FIB-sliced GLAD cross sections is planned to investigate the interesting nanometer-sized structural characteristics that have been reported for TEMs of individual GLAD nanorods.²⁸ Despite the resolution limitations, the data shown in Figure 11 may reveal some additional information about why some nanorods successfully out-compete their neighbors. Columns 2 and 3, which die out the earliest, have very few branches discernible at the resolution available. Columns 1 and 4, which survive to the tallest height, generally maintain many side arms. It may be that nanocolumns that grow branches of significant area are able to shadow their neighbors and steal incoming evaporant flux, thus ensuring their survival and growth at the expense of their neighbors. Investigation over a range of image resolution may yield more information.

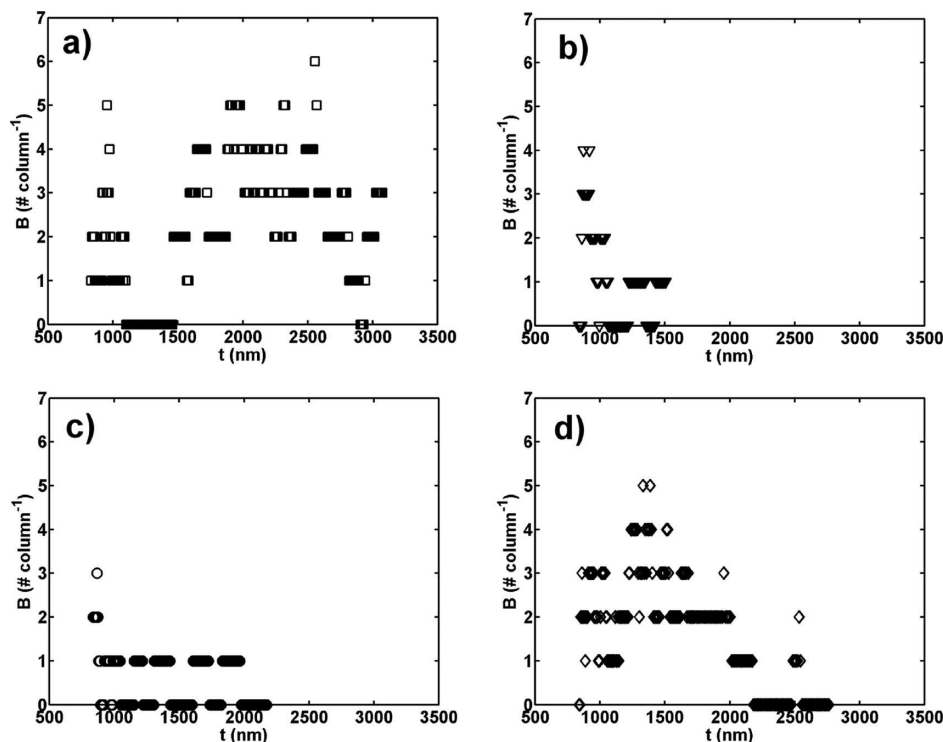


Figure 11. Numbers of branches as a function of nanorod height for nanorods (a) 1, (b) 2, (c) 3, and (d) 4. A large number of branches seem to correlate with nanorods that outgrow neighbors.

Conclusions

We have used FIB milling to slice and image the porous nanostructure deposited using the GLAD technique. By performing multiple slicing sequences, each at an increasing magnification and resolution, we were able to view the structure of a representative TiO_2 GLAD film over a range of sizes. Following postprocessing, which included image alignment and sequence stitching, we have been able to create a 3D reconstruction of the film. This reconstruction, the first of its kind, has allowed us to examine the porous, columnar, and bifurcated nature of the structure.

The identification of nanorods within the acquired cross sections has allowed for the measurement of column diameter and inter-nanorod spacing characteristics as a function of the GLAD film thickness. These parameters were found to follow a self-similar growth pattern, with growth scaling factors that indicate a faster growth rate of nanorod diameters than nanorod spacing. Tracking of individual nanorods also revealed some interesting trends in bifurcation and column survival. Further investigation involving

detailed transmission electron microscopy (TEM) imaging is also planned in order to study this relationship in more detail. Use of the FIB to section and view GLAD and other nanocolumnar thin film structures will be useful for understanding not only growth scaling and bifurcation properties but also porosity and roughness. We plan to continue to apply the FIB sectioning technique to understand the details of growth processes for a range of GLAD structures.

Acknowledgment. We acknowledge the financial support of the Natural Sciences and Engineering Research Council of Canada (NSERC), the Alberta Informatics Circle of Research Excellence (iCORE), Alberta Innovates: Technology Futures, Engineers Canada-Manulife Financial Scholarships, and Micralyne Inc. SEM and FIB-SEM experiments were supported by the National Research Council (NRC) National Institute for Nanotechnology (NINT). Use of the Integrated Nanosystems Research Facility at NINT, supported through the Canadian Foundation for Innovation (CFI) and NanoAlberta, is also acknowledged.